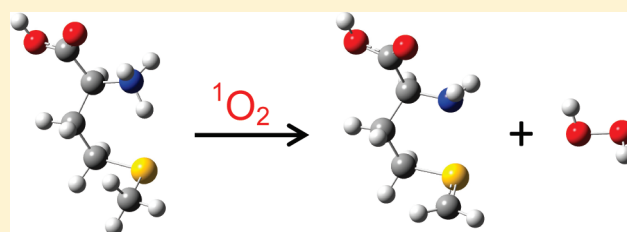


# Experimental and Trajectory Study on the Reaction of Protonated Methionine with Electronically Excited Singlet Molecular Oxygen ( $a^1\Delta_g$ ): Reaction Dynamics and Collision Energy Effects

Yigang Fang, Fangwei Liu, Andrew Bennett, Shamim Ara, and Jianbo Liu\*

Department of Chemistry and Biochemistry, Queens College and the Graduate Center of the City University of New York, 65-30 Kissena Boulevard, Flushing, New York 11367, United States

**ABSTRACT:** The reaction of protonated methionine with the lowest electronically excited state of molecular oxygen  $O_2(a^1\Delta_g)$  was studied in a guided ion beam apparatus, including the measurement of reaction cross sections over a center-of-mass collision energy ( $E_{col}$ ) range of 0.1–2.0 eV. A series of electronic structure and RRKM calculations were used to examine the properties of various complexes and transition states that might be important along the reaction coordinate. Only one product channel is observed, corresponding to generation of hydrogen peroxide via transfer of two hydrogen atoms (H2T) from protonated methionine to singlet oxygen. At low collision energies, the reaction approaches the collision limit and may be mediated by intermediate complexes. The reaction shows strong inhibition by collision energy, and becomes negligible at  $E_{col} > 1.25$  eV. A large set of quasi-classical direct dynamics trajectory simulations were calculated at the B3LYP/6-21G level of theory. Trajectories reproduced experimental results and provided insight into the mechanistic origin of the H2T reaction, how the reaction probability varies with impact parameter, and the suppressing effect of collision energy. Analysis of the trajectories shows that at  $E_{col} = 1.0$  eV the reaction is mediated by a precursor and/or hydroperoxide complex, and is sharply orientation-dependent. Only 20% of collisions have favorable reactant orientations at the collision point, and of those, less than half form precursor and hydroperoxide complexes which eventually lead to reaction. The narrow range of reactive collision orientations, together with physical quenching of  $^1O_2$  via intersystem crossing between singlet and triplet electronic states, may account for the low reaction efficiency observed at high  $E_{col}$ .



## I. INTRODUCTION

Electronically excited singlet molecular oxygen ( $^1O_2$ ,  $a^1\Delta_g$ ) is a reactive oxygen species important in fields from health and medicine to material sciences. It has a characteristic chemistry in which molecules are oxygenated, setting it apart from ground-state triplet oxygen ( $^3O_2$ ).<sup>1–6</sup>  $^1O_2$ -mediated oxygenation reactions are involved in cell death, aging, diseases,<sup>7</sup> photodynamic therapy for cancer,<sup>8</sup> and photochemical transformation of biological species in the atmosphere,<sup>9</sup> among others. It has been established that proteins are a major target for  $^1O_2$ -mediated oxidative damage in living bodies, with damage occurring preferentially at tryptophan (Trp), histidine (His), tyrosine (Tyr), methionine (Met), and cysteine (Cys) residues because these residues have electron-rich side chains and thus are favored by electrophilic oxidizers.<sup>7,10,11</sup> Of these five susceptible amino acids, methionine represents a special case.<sup>12</sup> Unlike oxidation of other amino acid residues, oxidative modification of methionine can be repaired by methionine sulfoxide reductases (MsrA and MsrB) that catalyze the thioredoxin-dependent reduction of methionine sulfoxide residues back to methionine residues—an evolutionary response to oxygen-induced damage in the Earth's atmosphere and in more localized environments.<sup>12,13</sup> Consequently, methionine residues act as an antioxidant pool, and the increase of oxidized methionine residues in proteins may reflect an increase

of  $^1O_2$  generation, decrease of oxidant scavengers, or loss of methionine sulfoxide reductases and other reducing equivalents involved. For this reason, methionine oxidation has been investigated extensively in biochemistry and biology, along with the photodynamic therapy on living bodies and in particular on proteins and enzymes.

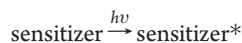
It is also worth noting that amino acids (free and combined forms) are ubiquitous in tropospheric particles and depositions,<sup>14–17</sup> and undergo transformations due to photochemically formed reactive oxygen species.<sup>9,18</sup> Because methionine can be quantitatively oxidized by  $^1O_2$  (it is a pure  $^1O_2$  chemical quencher) and other reactive oxygen species, the ratio of oxidized methionine/methionine can be used as a chemical marker for the transport and age of atmospheric particles and drops.<sup>9</sup> In addition, it was reported that oxidation of methionine results in nucleation and formation of particles, which accounts for a new route for aerosol production over remote marine areas.<sup>17</sup> These facts demonstrate the significance of methionine oxidation in atmospheric chemistry, in addition to biological milieu.

**Received:** December 23, 2010

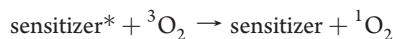
**Revised:** February 4, 2011

**Published:** February 28, 2011

Most experiments concerning the methionine oxidation mechanism were carried out in solution using photosensitization methods (often referred to as “photooxidation”), where  $^1\text{O}_2$  was generated upon exposure to ultraviolet or visible light in the presence of sensitizers,<sup>19</sup> i.e.,



followed by



Photooxidation of methionine shows complex features with several competing pathways and multiple products,<sup>3,7,10,11,20–26</sup> that are easily varied by many factors (e.g., pH, oxygen concentration, solvent composition, type of sensitizers, buffer ions). This is partly due to the fact that both type I (free radical-mediated)<sup>27–29</sup> and type II ( $^1\text{O}_2$ -mediated)<sup>4</sup> mechanisms might exist in photooxidation and simultaneously contribute to the reaction. Consequently, despite a few decades of studies, several fundamental aspects of methionine oxidation including products, stoichiometry, and intermediates involved have yet to be fully elucidated. To circumvent the problems associated with solution-phase photooxidation, oxidation experiments were reported using heterogeneous photosensitizers. For examples, sensitizers were immobilized on glass beads<sup>30,31</sup> or absorbed onto porous glass,<sup>32,33</sup> so that free sensitizers did not present in solution and singlet oxygen was delivered through space; accordingly, the oxidation of methionine proceeded predominantly via a type II mechanism.

In this paper, we report a detailed reaction dynamics study for protonated methionine ( $\text{MetH}^+$ ) and chemically generated, “clean”  $^1\text{O}_2$  in the gas phase using an electrospray-ionization (ESI)<sup>34,35</sup> guided ion beam scattering<sup>36</sup> apparatus, including reaction cross section measurement over a wide range of collision energies ( $E_{\text{col}}$ ). Compared to the study of  $^1\text{O}_2$  reactions in solution, much less is known about the ion chemistry with  $^1\text{O}_2$  in the gas phase. To the best of our knowledge, there are only a few ion–molecule reaction studies involving  $^1\text{O}_2$ ,<sup>37–50</sup> mostly concentrating on reactions of small negative ions with  $^1\text{O}_2$  using a selected ion flow tube by Viggiano and co-workers.<sup>44–50</sup> To supplement our gas-phase experimental study, extensive theoretical approaches were employed. Quantum chemistry calculations were used to locate intermediate complexes and transition states along the reaction coordinate; then, Rice–Ramsperger–Kassel–Marcus (RRKM) theory<sup>51</sup> was used to predict their properties. Finally, quasi-classical direct dynamics trajectory simulations were used to provide additional mechanistic insights.

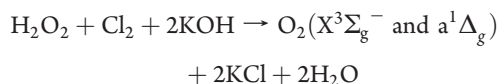
## II. EXPERIMENTAL AND COMPUTATIONAL DETAILS

**A. Experimental Procedures.** The guided ion beam tandem mass spectrometer used in the present experiment has been described in detail previously,<sup>37,52,53</sup> along with our operation, calibration, and data analysis procedures. Briefly, the apparatus consists of an ion source, radio frequency (rf) hexapole ion guide, quadrupole mass filter, rf octopole ion guide surrounded by a scattering cell, second quadrupole mass filter, and a pulse-counting detector. Both quadrupole mass filters use Extrel 9.5 mm trifilter rods. In order to achieve high ion transmission and mass resolution for this system, both mass filters were operated at 2.1 MHz (Extrel model 150 QC) with a mass/charge ( $m/z$ ) range of 1–500.

The sample solution was prepared in HPLC grade methanol and water (1:1 volume ratio) containing  $5 \times 10^{-4}$  M methionine ( $\geq 99.5\%$ , Sigma) and  $5 \times 10^{-4}$  M hydrochloric acid (Riedel-de Haën). The solution was sprayed into the ambient atmosphere through an electrospray needle using a syringe pump (KdScientific model 100), at a constant flow rate of 0.04 mL/h. The electrospray needle was prepared from 35-gauge hypodermic stainless steel tubing (0.13 mm o.d.  $\times$  0.06 mm i.d., Small Parts Inc.), and biased at 3200 V relative to ground. Positively charged droplets formed from the electrospray needle were fed into a heated desolvation capillary assembly. The capillary was biased at 70 V relative to ground and heated to 170 °C. Charged liquid droplets and solvated ions underwent continuous desolvation as they passed through the heated capillary,<sup>54</sup> converting to gas-phase ions and transported into the source chamber. A skimmer with an orifice diameter of 1.5 mm was located 2.5 mm from the capillary end, separating the ion source chamber and the hexapole ion guide. The skimmer was biased at 10 V relative to ground, and the electrical field between the capillary and skimmer helped remove remaining solvent molecules attached to ions by collision-induced desolvation.<sup>54</sup> Ions emerging from the skimmer were passed into a rf hexapole ion guide at a pressure of 15 mTorr, resulting in collisional focusing and thermalization of internal and translational energies of ions.<sup>55–57</sup> In a previous study,<sup>37</sup> we measured the cross sections for collision-induced dissociation (CID) of  $\text{Na}^+$  (proline) with  $\text{Xe}$ <sup>55,58</sup> as a function of  $E_{\text{col}}$ , and fitted the energy dependence of CID cross sections using the modified line-of-centers model.<sup>59–61</sup> The best fit vibrational energy of primary ions corresponded to a vibrational temperature of 310 K, suggesting that primary ions were thermalized via ion-neutral collisions in the hexapole ion guide and their internal energy can be well-defined using a Maxwell–Boltzmann distribution.

Ions subsequently passed into a set of entrance focusing lenses followed by the first quadrupole mass filter for mass selection. Mass-selected ions were injected into an octopole ion guide, which trapped ions in the radial direction. The octopole ion guide operated at 2.6 MHz with a peak-to-peak amplitude of 700 V. DC bias voltage was applied to the ion guide with variable amplitude. The DC bias voltage was used in the retarding potential analysis (RPA)<sup>62</sup> to determine the initial kinetic energy of selected ions; i.e., the intensity of the primary ion beam was measured while sweeping the octopole bias. The DC bias voltage also allowed control of the kinetic energy ( $E_{\text{lab}}$ ) of ions in the laboratory frame, thereby setting the collision energy ( $E_{\text{col}}$ ) between ions and reactant gas molecules in the center-of-mass frame, i.e.,  $E_{\text{col}} = E_{\text{lab}} \times m_{\text{neutral}} / (m_{\text{ion}} + m_{\text{neutral}})$ , where  $m_{\text{neutral}}$  and  $m_{\text{ion}}$  are the masses of neutral and ionic reactants, respectively. The octopole guided ions through a scattering cell filled with neutral reactant gas. The scattering cell pressure was measured by a capacitance manometer (MKS Baratron 690 head and 670 signal conditioner). Unreacted  $\text{MetH}^+$ , together with any product ions, were collected by the ion guide, and passed into a second quadrupole mass filter for mass analysis and counted using an electron multiplier. The  $\text{MetH}^+$  ion beam intensity was  $4 \times 10^5$  ion/s and constant within 10%. The initial kinetic energy of the primary ion beam was around 1.0 eV, determined by the RPA method, and the energy spread was 0.3–0.4 eV. This corresponds to an energy spread of 0.07 eV in the center-of-mass frame for the collision of  $\text{MetH}^+$  with  $^1\text{O}_2$ . Reaction cross sections were calculated from the ratio of product and reactant ion intensities,  $^1\text{O}_2$  pressure, and the calibrated effective length of the scattering cell.<sup>37</sup>

One feature of this system is that the neutral reactant  $^1\text{O}_2$  is an electronically excited state. In our previous experiment,<sup>37</sup>  $^1\text{O}_2$  ( $a^1\Delta_g$ ) was generated by microwave discharge<sup>63,64</sup> in an  $\text{O}_2/\text{Ar}$  mixture, and the  $^1\text{O}_2$  yield was estimated using the specific energy deposition per molecule in the discharge.<sup>65</sup> Microwave discharge not only produced  $^1\text{O}_2$  ( $a^1\Delta_g$ , 2.5–9%) but also produced O atoms and  $\text{O}_3$  as well. We used a mercuric oxide coating inside the discharge tubing to remove O atoms via their recombination. However, there are environmental restrictions on mercury use. Besides problems associated with O atoms,  $\text{O}_3$  (<1%)<sup>44</sup> may react with biomolecules, causing uncertainties in reaction measurements. For this system, we employed a chemical  $^1\text{O}_2$  ( $a^1\Delta_g$ ) generator based on the following reaction<sup>66,67</sup>



This chemical  $^1\text{O}_2$  generation technique was to create oxygen–iodine lasers<sup>68</sup> and was recently introduced to ion–molecule reactions with  $^1\text{O}_2$  by Viggiano and co-workers.<sup>45,46,48–50</sup> We adopted a similar procedure used by Viggiano et al. In the experiment, 20 mL of 35 wt %  $\text{H}_2\text{O}_2$  (Acros Organics) was very slowly mixed with 13 mL of 8.0 M KOH (>85%, Fisher Chemical) solution in a sparger that was immersed in a cold bath. The cold bath was maintained at  $-19^\circ\text{C}$  by a Lauda RP890 recirculating chiller. The resulting solution was held at  $-20^\circ\text{C}$  to lower the vapor pressure of the solution and prevent decomposition of  $\text{H}_2\text{O}_2$ , and was degassed before the reaction. A continuous flow of He (T.W. Smith, research grade) was first introduced to the slushy  $\text{H}_2\text{O}_2/\text{KOH}$  mixture at a flow rate of 50 sccm to prevent freezing of the mixture at the exit of the fritted gas aerator inside the sparger.  $\text{Cl}_2$  (Sigma-Aldrich,  $\geq 99.5\%$ ) was then added, mixing with He in a gas proportioner (Matheson model 7300) at a flow rate of 2–3 sccm, and then bubbled through the  $\text{H}_2\text{O}_2/\text{KOH}$  solution. All the  $\text{Cl}_2$  reacted to form the ground-state and excited  $\text{O}_2$ .<sup>46</sup> Water vapor in the resulting gas mixture was removed by a second cold trap after the reactor that was kept at  $-70^\circ\text{C}$  using a methanol/water/dry ice slush bath. Using this generation technique, only ground state  $\text{O}_2$ ,  $\text{O}_2$  ( $a^1\Delta_g$ ), and He remained in the downstream gas flow and were introduced to ion–molecule reactions, thus eliminating O and  $\text{O}_3$  contaminants.

Before leaking into the scattering cell, the gases flowed through a stainless steel emission cell (2.54 cm i.d. and 10 cm length), where the emission of  $\text{O}_2$  ( $a^1\Delta_g \rightarrow X^3\Sigma_g^-, \nu = 0-0$ ) at 1270 nm was detected.<sup>69,70</sup> The emission cell has a glass window in the front and a silver-coated concave reflective mirror (ThorLabs CM254-050-P01,  $f = 50$  mm) at the end. The emission cell was continuously pumped through a pressure control valve (Cole-Parmer model R-68027-78 with an integrated PID) to maintain emission cell pressure at 15 Torr (measured using a MKS 626B Baratron manometer). This pressure was chosen to reduce the residence time and, hence, the wall quenching of  $^1\text{O}_2$  inside the cold traps, gas tubing, and emission cell, so that maximum emission intensity could be detected. The emission detection system consists of a 5 nm bandwidth interference filter centered at 1270 nm (Andover, blocked to  $1.55 \mu\text{m}$ ), an optical chopper (SRS model SRS40), a thermo-electrically cooled InGaAs photodetector (Newport model 71887 detector and 77055 TE-cooler controller), and a digital dual phase lock-in amplifier (SRS model SR830).<sup>44,64,71</sup>  $^1\text{O}_2$  emission from the emission cell was collected by a plano-convex BK7 lens (ThorLabs LA1805,  $f = 30$  mm),

passed through the optical chopper and the interference filter. The chopped emission was focused by another plano-convex BK7 lens (ThorLabs, LA1131,  $f = 50$  mm, AR coated for 1050–1620 nm) into the InGaAs detector, and the signal was measured by the lock-in amplifier. Our detection system has not been calibrated, so we could not determine the absolute emission intensity. Since we adopted a very similar production procedure as Viggiano et al.'s, we assumed the maximum emission intensity detected corresponds to a 15%  $^1\text{O}_2$  yield in the total oxygen flow as reported by Viggiano et al.<sup>45,47,50</sup> Because the intensity of emission linearly depends on  $^1\text{O}_2$  concentration, the change of the  $^1\text{O}_2$  yield during the experiment could be monitored by measuring the emission.  $^1\text{O}_2$  pressure in the scattering cell is the product of the total gas pressure in the scattering cell, the percent of  $\text{Cl}_2$  (assumed to completely convert to  $\text{O}_2$ <sup>46</sup>) in the  $\text{Cl}_2 + \text{He}$  flow, and the  $^1\text{O}_2$  yield in the oxygen product. To check how reliable our determination of  $^1\text{O}_2$  pressure in the scattering cell was, we measured the reaction cross section ( $\sigma_{\text{Chem-O}_2}$ ) of protonated tyrosine +  $^1\text{O}_2$  using the same procedure just described and then compared it to our previous measurement ( $\sigma_{\text{MW-O}_2}$ ) which relied on a microwave discharge method to generate  $^1\text{O}_2$ , and the  $^1\text{O}_2$  yield was estimated using the specific energy deposition per molecule during the discharge. A good agreement (i.e.,  $(\sigma_{\text{Chem-O}_2} - \sigma_{\text{MW-O}_2})/\sigma_{\text{Chem-O}_2}$  is within  $\sim 35\%$ ) was found, taking into account the combined errors in two experiments.

The collision cross section ( $\sigma_{\text{collision}}$ ), taken as the greater of the ion-induced dipole capture cross section ( $\sigma_{\text{capture}}$ )<sup>72</sup> and hard-sphere collision cross section ( $\sigma_{\text{hard-sphere}}$ ), is about 40–50  $\text{\AA}^2$  for  $\text{MetH}^+ + \text{O}_2$  (He).  $\sigma_{\text{hard-sphere}}$  is calculated from the orientation-averaged contact radii of  $\text{MetH}^+$  and  $\text{O}_2$  (or He), and exceeds  $\sigma_{\text{capture}}$  for  $E_{\text{col}} > 0.2$  eV. The pressure of  $\text{O}_2/\text{He}$  in the scattering cell was maintained at 0.25–0.29 mTorr to provide a reasonable intensity of product ion signal, while keeping multiple collision effects at an insignificant level. In this range of pressure, the probability of  $\text{MetH}^+$  ions undergoing a single collision is  $\sim 14\%$ , and that of double collisions is  $< 2\%$ . The majority of  $\text{MetH}^+$  ions (>84%) passed through the scattering cell without any interaction with  $\text{O}_2$  or He.

Because the signals we measured are small, it is important to minimize systematic variation in experimental conditions that might be caused by drifting potentials, changes in ion beam intensities,  $^1\text{O}_2$  yields, etc. The intensity of  $^1\text{O}_2$  emission was monitored continuously during the whole experiment and signal variation (controlled to within 20%) was corrected for ion–molecule cross section. RPA measurements of primary ions were performed before and after each experiment to check the initial kinetic energy of the primary ion beam. To check the reproducibility, the entire experiment was repeated several times and each time we cycled through different collision energies. On the basis of the reproducibility of the cross section measurements taken over a four-week period, we estimate that the relative error is  $< 20\%$ . To check the reactivity of  $\text{MetH}^+$  toward ground-state  $\text{O}_2$  and He, control experiments were performed under the same conditions except that  $\text{Cl}_2$  was replaced by oxygen gas at the same flow rate.

**B. Computational Methods.** To aid in reaction coordinate interpretation, density function theory (DFT) electronic structure calculations were performed at the B3LYP/6-31+G\* level of theory, using Gaussian 03.<sup>73</sup> Geometries were optimized calculating the force constants at every step. Vibrational frequencies and zero-point energies (ZPE) were scaled by a factor of 0.9613 and 0.9804,<sup>74</sup> respectively. All the transition states (TSs) found

were verified as first-order saddle points by frequency calculations, and the vibrational mode with the imaginary frequency corresponds to the reaction pathway. RRKM rates and density of states were done with the program of Zhu and Hase,<sup>75</sup> using its direct count algorithm, and scaled frequencies and energetics from the DFT calculations.

Quasi-classical, direct dynamics trajectories were calculated using the chemical dynamics program VENUS99 of Hase et al.<sup>76</sup> to set up the trajectory initial conditions, and the Hessian-based method of Bakken et al.<sup>77</sup> implemented in Gaussian 03 to propagate each trajectory, with Hessians recalculated every five steps. The integrations were performed with a step size of 0.25 amu<sup>1/2</sup> bohr ( $\sim 0.4$  fs), which conserved the total energy to better than  $10^{-4}$  Hartree. The SCF = XQC option was adopted during trajectory integration so that a quadratically convergent Hartree–Fock (QC-SCF) method<sup>73,78</sup> was used in case the usual but much faster, first-order SCF method did not converge within the allotted number of cycles. Because millions of gradients and Hessian evaluations were required, the level of theory used was necessarily modest. To select a suitable level of theory, we performed relaxed potential energy surface (PES) scans for approach of <sup>1</sup>O<sub>2</sub> to MetH<sup>+</sup> in several different orientations using MP2 and B3LYP methods with 6-21G, 6-31G, and 6-31+G\* basis sets. The MP2 method ran into convergence problems for this system. At the B3LYP level of theory, the calculated MetH<sup>+</sup> – <sup>1</sup>O<sub>2</sub> interaction is largely attractive. The MetH<sup>+</sup> – <sup>1</sup>O<sub>2</sub> potential energy surface has a broad, shallow (0.2–0.3 eV) electrostatic well at long range (3.5–4.0 Å center-of-mass distance), before trapping into a product-like complex well ( $\sim 1$  eV). The shapes of attractive wells are in reasonable agreement for different basis sets. The major difference is that the well becomes less deep for B3LYP/6-31G, amounting to a decrease of 0.3 eV binding energy at the global minima in the PES. B3LYP/6-21G tracks the B3LYP/6-31+G\* approach energy curve much better. We also calculated several reactive and nonreactive trajectories at B3LYP/6-31+G\*, and for each trajectory selected several geometries corresponding to chemically important steps in the collision: reactants, products, points where bonds appear to be breaking or forming in various orientations. The energies for these selected geometries were then calculated at candidate levels of theory (including B3LYP/6-21G, B3LYP/6-31G, and B3LYP/6-31G\*) and compared to B3LYP/6-311++G\*\* and QCISD/cc-pVDZ energies. On the basis of the overall level of agreement and computational speed, we chose the B3LYP/6-21G level of theory for the main set of trajectories.

The initial conditions for the trajectories were chosen to mimic the conditions of our experiment. Because MetH<sup>+</sup> ions were thermalized in the experiment, their initial vibrational and rotational energies were sampled from Boltzmann distributions at 300 K. Similarly, <sup>1</sup>O<sub>2</sub> in the experiment was close to room temperature, so 300 K was used for both the rotational and vibrational temperature for <sup>1</sup>O<sub>2</sub>. The quasi-classical initial vibrational state was simulated by giving each reactant atom displacement from equilibrium and momentum appropriate to the initial rovibrational state, with random phases for different modes. Both MetH<sup>+</sup> and <sup>1</sup>O<sub>2</sub> have zero-point energy in all vibrational modes. Randomly oriented MetH<sup>+</sup> and <sup>1</sup>O<sub>2</sub> were given relative velocities corresponding to the collision energy of 1.0 eV. This  $E_{\text{col}}$  was chosen for several considerations. First, although the low energy regime is more closely relevant to biological situations, the trajectory time at low  $E_{\text{col}}$  might be too long to follow trajectories to completion. This was confirmed by a limited set of

trajectories that ran at  $E_{\text{col}} = 0.5$  eV. At  $E_{\text{col}} = 1.0$  eV, the lifetime of the collision intermediate decreases but the complex still plays a role in this transition regime before the direct mechanism dominates completely (see trajectory results below). Second, at  $E_{\text{col}} = 1.0$  eV, the reaction cross section is not very small, making it possible to generate enough reactive trajectories needed for statistical analysis. Third, the quasi-classical trajectory (QCT) method we used is not applicable to nonadiabatic collisions; i.e., it does not allow nonadiabatic transitions at surface crossing seams.<sup>37,79,80</sup> On the other hand, at higher  $E_{\text{col}}$ , there may exist two electronic states contributing to the lowest Born–Oppenheimer potential surface that the trajectory runs on, and the system may possibly proceed from <sup>1</sup>MetH<sup>+</sup> + <sup>1</sup>O<sub>2</sub> to <sup>3</sup>MetH<sup>+</sup> + <sup>3</sup>O<sub>2</sub> as reactants separate. The excitation energy of <sup>3</sup>MetH<sup>+</sup> is calculated to be 2.33 eV more than that of <sup>1</sup>O<sub>2</sub> at the B3LYP/6-21G level of theory used for trajectory calculations. Therefore, we have to run trajectories well below the energy threshold for intersystem crossing, so that the nonadiabatic transitions can be avoided.

Batches of trajectories (100 each) were calculated for discrete values of the reactant impact parameter ( $b = 0.1, 0.5, 1.0, 1.5, 2.0, 2.5, 3.0, 4.0,$  and  $5.0$  Å) rather than randomly sampling the  $b$  distribution, allowing us to examine the  $b$  dependence of the scattering dynamics in detail. At  $b = 5.0$  Å, the angular deflection and energy transfer are already small, and no reactive trajectories were observed. The random number generator seed used in setting up initial conditions for each batch of trajectories was identical.<sup>79,80</sup> Each trajectory batch, therefore, used the same pseudorandom sequence to sample the reactant parameters (orientations, rotational and vibrational energies, vibrational phases, etc.). As a result, it is easy to compare trajectories for different impact parameters, because, except for the impact parameter being varied, corresponding trajectories from different batches have identical initial conditions. The error from inadequate sampling of reactant parameter space is the same for all batches, and tends to cancel when comparing batches for different impact parameters.

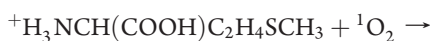
All trajectories started with an initial center-of-mass reactant separation of 9.0 Å, and were terminated either when the distance between the final products exceeded 8.5 Å or after 2000 steps. The error in the energy due to the long-range potential at 9 Å is less than 3 meV. A total of 900 trajectories were calculated, and the time for one trajectory varied from 140 to 220 CPU hours on an Intel core quad (3.0 GHz)-based cluster. For trajectory visualization, we used the program gOpenMol.<sup>81</sup> Detailed analysis of individual trajectories and statistical analysis of the trajectory ensemble was done with programs written for this purpose, as described previously.<sup>37,79,82–85</sup>

One obvious issue with using the QCT method to probe dynamics is that vibrational energy is not quantized and thus ZPE is not conserved. At the start of the trajectories, vibrational energy is partitioned appropriately to represent the initial internal temperature. Lack of quantization allows unphysical distribution of energy between vibrational modes during and after collisions,<sup>86,87</sup> including having trajectories where the final  $E_{\text{vib}}$  is below the ZPE. Because we ran trajectories at a high  $E_{\text{col}}$ , such obviously unphysical behavior was not observed in trajectories. We note that the purpose of our trajectory simulations was to probe the gross features of the reaction mechanism, particularly at early times in the collisions; thus, errors from classical treatment of the nuclear motions were likely minimal. In the final analysis, a useful test is how well the trajectories reproduce

experimental measured cross sections, and as shown below, the agreement is good.

### III. RESULTS AND DISCUSSION

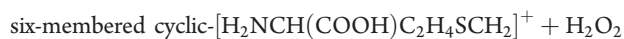
**A. Reaction Cross Section and Comparison to Solution-Phase Results.** For the reaction of  $\text{MetH}^+$  ( $m/z$  150) +  $^1\text{O}_2$ , product ions were observed at  $m/z$  148 over the collision energy range of 0.1–2.0 eV. At high collision energies, product ions were also observed at  $m/z$  133 and 104. The latter two product ion masses correspond to the elimination of  $\text{NH}_3$  and of  $\text{H}_2\text{O} + \text{CO}$ , respectively, from  $\text{MetH}^+$ , with the loss of  $\text{H}_2\text{O} + \text{CO}$  increasing in importance with increasing collision energy.  $[\text{MetH}^+ - \text{NH}_3]$  and  $[\text{MetH}^+ - (\text{H}_2\text{O} + \text{CO})]$  are attributed to collision-induced dissociation,<sup>88–92</sup> and were observed upon collisions with ground-state  $\text{O}_2$  and Ar, too. In addition, CID product ions at  $m/z$  132 ( $[\text{MetH}^+ - \text{H}_2\text{O}]$ ) and 102 ( $[\text{MetH}^+ - \text{CH}_3\text{SH}]$ ) showed up at high collision energies, in agreement with previous CID studies.<sup>88–92</sup> Product ions of  $m/z$  148, on the other hand, were not observed with ground-state  $\text{O}_2$ , Ar, or He. This product channel corresponds to transfer of two hydrogen atoms from protonated methionine to form hydrogen peroxide ( $\text{H}_2\text{O}_2$ ) with  $^1\text{O}_2$ , and is referred to as the H2T channel. We also looked at  $\text{MetH}^+ + ^1\text{O}_2$  over the same collision energy range but used microwave discharge generated  $^1\text{O}_2$ .<sup>37</sup> Similar product ions were observed. There are various H2T routes leading to three possible product ions, indicated below. The structures for these product ions are given in Figure 4, and the corresponding values of  $\Delta H_{\text{rxn}}$  are derived from B3LYP/6-31+G\* calculations. In principle, the  $m/z$  148 product ions could also be produced through elimination of  $\text{H}_2$  via CID of  $\text{MetH}^+$ . However, we can discount this probability, except at high  $E_{\text{col}}$ , since the CID thresholds are calculated to be 1.1–2.0 eV for these product ions.



$$\text{(labeled P1)} \Delta H_{\text{rxn}} = -0.55 \text{ eV}$$



$$\text{(labeled P2)} \Delta H_{\text{rxn}} = -0.86 \text{ eV}$$



$$\text{(labeled P3)} \Delta H_{\text{rxn}} = -1.52 \text{ eV}$$

The reaction cross sections for the H2T channel are given in Figure 1, over the center-of-mass  $E_{\text{col}}$  range of 0.1–2.0 eV. Note that the absolute values of cross sections were calculated on the basis of the assumption that the maximum  $^1\text{O}_2$  yield from the chemical  $^1\text{O}_2$  generator is 15%;<sup>45,47,50</sup> there may, therefore, exist uncertainty concerning absolute cross sections. However, based on the fact that methionine is highly reactive toward  $^1\text{O}_2$ , and the measured reaction cross sections at  $E_{\text{col}} = 0.2$  eV ( $36 \text{ \AA}^2$ ) are close to the collision cross section ( $44 \text{ \AA}^2$ ), we believe that the values of reaction cross sections were reasonably estimated. More importantly, this source of uncertainty does not affect the relative cross sections, i.e., the collision energy dependence of cross section, which is our primary interest here. The relative uncertainty is estimated to be  $\sim 20\%$ . The reaction is strongly suppressed by collision energy at low  $E_{\text{col}}$ , becoming negligible at  $E_{\text{col}} > 1.25$  eV.

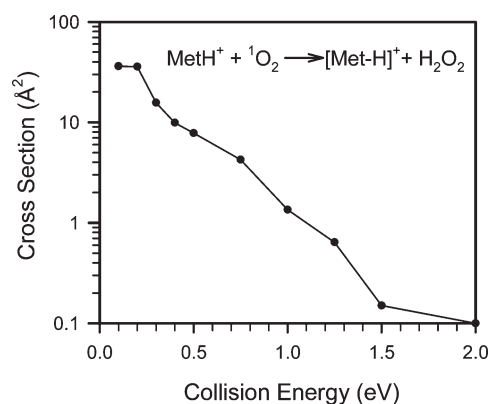


**Figure 1.** Cross sections for production of  $\text{H}_2\text{O}_2$  from the reaction of protonated methionine with  $^1\text{O}_2$ , as a function of center-of-mass collision energy.

Note that various CID channels, because of their endoergicities, do not significantly interfere with the H2T channel at low energies. Cross sections level off at the lowest  $E_{\text{col}}$ . This is most likely artificial, due to the low collection efficiency of slow product ions at our lowest  $E_{\text{col}}$ . On the basis of the estimated cross section values, reaction efficiency ( $=\sigma_{\text{reaction}}/\sigma_{\text{collision}}$ ) is around 55–82% at  $E_{\text{col}} = 0.1$ –0.2 eV, 30% at 0.3 eV, 10% at 0.5 eV, and less than 5% at 1.0 eV and greater. The low efficiency at high  $E_{\text{col}}$  may reflect the competition between chemical reaction and physical quenching of  $^1\text{O}_2$ , as well as possible bottlenecks in dynamics.

Production of  $\text{H}_2\text{O}_2$  from the reaction of methionine with  $^1\text{O}_2$  has been reported in solution-phase photooxidation,<sup>3,21,23</sup> and was rationalized by secondary reactions of an intermediate persulfoxide. As shown in Figure 2, secondary reactions are pH-dependent. At high pH (above 9), the reaction involves attack of  $\text{OH}^-$  at the sulfur atom of persulfoxide, i.e., path (a) in the figure. The displacement reaction gives one molecule of sulfoxide and one molecule of  $\text{H}_2\text{O}_2$ . At the intermediate pH range of 6–10, when methionine carries a free amino group, path (b) becomes dominant, leading to dehydromethionine via internal displacement. The structure of dehydromethionine was assigned as a five-membered heterocyclic N–S compound.<sup>93</sup>  $\text{H}_2\text{O}_2$  is also produced in this process. At pH below 6, the persulfoxide intermediate oxidizes a second methionine molecule by the sulfide trapping mechanism, resulting in a stoichiometry of  $2\text{Met} + ^1\text{O}_2 \rightarrow 2$  methionine sulfoxide (MetO).<sup>10,11,32</sup> Competition among these processes in the photooxidation of methionine accounted for the variation in  $\text{O}_2$  uptake observed in solution-phase experiments; i.e., the methionine to  $^1\text{O}_2$  ratio is 1:1 above pH 7 and 2:1 below pH 5.<sup>21</sup> On the basis of solution-phase results, formation of dehydromethionine and  $\text{H}_2\text{O}_2$  via path (b) requires a free amino group basic enough to nucleophilically attack sulfur, and therefore could not occur with protonated methionine.<sup>23</sup> In fact, the measured contribution of path (b) became negligible at pHs lower than the  $\text{pK}_a$  ( $=9.2$ ) of the ammonium group. Therefore, alternative pathways must be located to make gas-phase reaction results of  $\text{MetH}^+ + ^1\text{O}_2$  explicable.

**B. Reaction Coordinate at Low  $E_{\text{col}}$ .** Protonated methionine may exist in various geometric conformations resulting from the flexibility of its structure. To find the global minimum of its conformational landscape, we applied a grid search method.<sup>94</sup> Since we are only interested in low-energy conformations, we assumed a *syn*-configuration of the carboxylic acid group and a

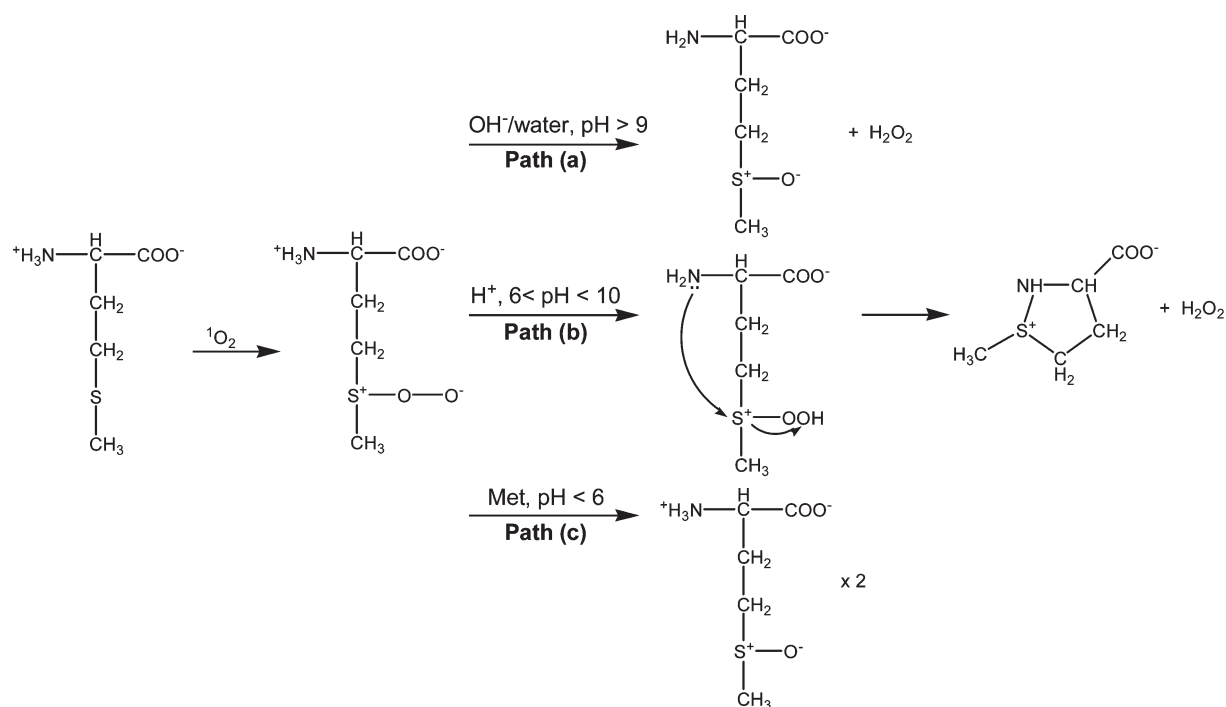


**Figure 2.** Reaction paths for photooxidation of methionine in solution: (a)  $\text{OH}^-$  displacement, (b) internal displacement, and (c) formation of two sulfoxide molecules.<sup>23</sup>

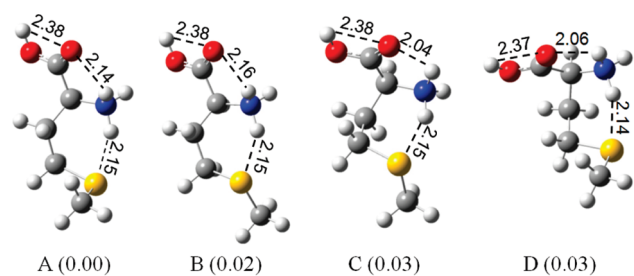


**Figure 3.** Low-lying conformations of protonated methionine calculated at B3LYP/6-31+G\*. Their relative energies at 0 K (including ZPE) are indicated in parentheses. The bond distances are shown in angstroms.

bifurcated  $\text{NH}_3^+ \cdots \text{O}=\text{C}$  intramolecular hydrogen bond in  $\text{MetH}^+$ .<sup>95</sup> Furthermore, the  $\alpha$ -amino nitrogen is assumed to be the preferred protonation site for methionine.<sup>96–98</sup> We systematically rotated each of the torsion angles along the methionine side chain through  $360^\circ$  at  $60^\circ$  increments to generate all possible conformations. Every conformation so generated was subjected to geometry optimization using Gaussian 03 to derive the associate minimum energy conformation. Many of the initial conformations optimized to the same minimum energy structure, and the four lowest energy conformations (within 0.1 eV) were found at the B3LYP/6-31+G\* level of theory. Their structures and relative energies at 0 K (including ZPE) are summarized in Figure 3. These low-lying conformations have strong intramolecular  $\text{C}=\text{O} \leftarrow \text{NH}_3^+ \rightarrow \text{S}$  charge complexation and hydrogen bond interactions, with a distance of 2.14–2.15 Å between the S atom and the closest H atom of the ammonium group and distances of 2.04–2.16 and 2.37–2.38 Å from the carbonyl O atom to the closest H of  $\text{NH}_3^+$  and to the hydroxyl H, respectively. The next group of stable conformations, with weak

$\text{C}=\text{O} \leftarrow \text{NH}_3^+ \rightarrow \text{S}$  interactions, lie 0.2 eV higher in energy with respect to conformations, A–D, in Figure 3. Our low energy conformations, A–D, are consistent with those found by Carl et al.<sup>99</sup> and Bleiholder et al.<sup>97</sup> using simulated annealing techniques and by Lioe et al.<sup>98</sup> using Monte Carlo simulations. According to Carl et al.'s infrared multiphoton dissociation experiment,<sup>99</sup> conformations A–D account for all populations of  $\text{MetH}^+$  at 298 K. Our subsequent calculations of the reaction coordinate focused on the lowest energy conformation, i.e., conformation A. It is certainly possible that interconversion between conformations A, B, C, and D might occur during the collision. It seems unlikely, however, that different conformations of amino acids would significantly change their reaction coordinate, and our trajectory simulations of  $\text{TyrH}^+ + {}^1\text{O}_2$ <sup>37</sup> and  $\text{MetH}^+ + {}^1\text{O}_2$  confirm this conclusion.

DFT calculation results for the reaction coordinate of  $\text{MetH}^+ + {}^1\text{O}_2$  are summarized in Figure 4, with reactants shown at zero energy. All energetics are calculated at the B3LYP/6-31+G\* level of theory. The details of the geometries for complexes, TSs, and products are available by request to the corresponding author. Two weakly bound complexes (complexes RC and PC) and two covalently bound complexes (hydroperoxides H\_1 and H\_2) were found. We attempted to locate transition states connecting the complexes to each other and to the products, as shown in Figure 4. Complex RC can be characterized as a reactant-like complex, formed by electrostatic interaction and ionic hydrogen bond. This complex has the  $\text{O}_2$  moiety sandwiched between the ammonium group and the sulfur atom of  $\text{MetH}^+$ , with distances of 2.28 and 1.64 Å for  $\text{O}-\text{O} \cdots \text{S}$  and  $\text{O}-\text{O} \cdots \text{H}_3\text{N}^+$ , respectively. The binding energy of RC is 0.38 eV with respect to the reactants. Because no rearrangement is required to form a reactant-like complex, it is unlikely that there would be significant activation barriers inhibiting formation of this complex. This conclusion was confirmed by a relaxed potential energy scan

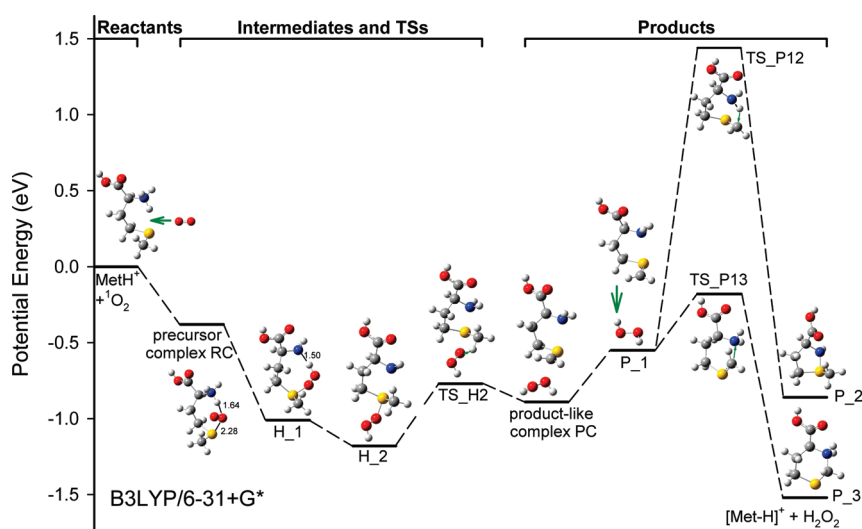


**Figure 4.** Schematic reaction coordinate for protonated methionine and  $\text{O}_2$  ( $a^1\Delta_g$ ). Energies of complexes, TSs, and products, relative to reactants, are derived from B3LYP/6-31+G\* values, including ZPE. The bond distances are shown in angstroms.

running along the dissociation of this complex back to the reactants. We note that, because of a lack of directional covalent or hydrogen bonds between  $\text{MetH}^+$  and  $\text{O}_2$ , complex RC will not have a well-defined geometry at the energies available in our experiment. This complex is rather floppy, with a large amplitude of intermolecular motion. The significance of this complex is that it allows repeated encounters between reactants, increasing the probability of transition to hydroperoxide intermediates. To this extent, complex RC is referred to as “precursor complex” in the following discussion.

Hydroperoxide  $\text{H}_1$  is a covalently bound intermediate  $\text{Met}(\text{OO})\text{H}^+$ , which was observed in trajectory simulations (see below). Attempts to optimize intermediate complexes corresponding to persulfoxide (i.e., without transfer of a H atom from  $-\text{NH}_3^+$  to  $-\text{SOO}$ ) converged, instead, to  $\text{H}_1$ . This indicates an absence of barrier for intramolecular proton transfer from the ammonium group to the  $\text{H}_1$  persulfoxide group. According to Mulliken charge population analysis, the  $-\text{SOOH}$  group carries most of the positive charge (more than 0.9). This demonstrates that an oxidation-induced post-translational modification could not only affect the local proton affinity of amino acid but also changes the site of protonation. It has been reported that oxidation of  $\text{MetH}^+$  to methionine sulfoxide ( $\text{MetOH}^+$ ) results in an increase in proton affinity, due to two factors: (1) higher intrinsic proton affinity and stronger ionic hydrogen bonding of the sulfoxide group than the sulfide group and (2) an increase in the ring size formed through charge complexation by the sulfoxide group, which allows more efficient hydrogen bonding compared to the sulfide group.<sup>96,100</sup> As a result, the proton in  $\text{MetOH}^+$  is equally hydrogen bonded to the amino and sulfoxide group. A similar scenario could happen for hydroperoxide  $\text{H}_1$ , where an eight-membered ring forms a strong hydrogen bond, stabilizing the proton more tightly. Consequently, the proton in  $\text{H}_1$  is located much closer to the persulfoxide group (1.04 Å) than to the amino group (1.50 Å). Hydroperoxide  $\text{H}_2$  is an analogue of  $\text{H}_1$ , except that the hydroperoxide group swings away from the amino group. The energy of  $\text{H}_2$  (−1.18 eV) is slightly lower than that of  $\text{H}_1$  (−1.01 eV), presumably because of the strong S–N bond in  $\text{H}_2$  (the S–N bond length is 2.4 Å in  $\text{H}_2$  vs 3.87 Å in  $\text{H}_1$ ). We ran trajectory simulations for  $\text{H}_1$  for several

picoseconds at the HF/3-21G level of theory, with randomly distributed internal energy equivalent to what  $\text{H}_1$  would have in reaction. During the trajectory time,  $\text{H}_1$  interconverts with  $\text{H}_2$  rapidly. Complex PC is product-like, in that two hydrogen atoms have been transferred to  $\text{O}_2$ , leaving  $\text{H}_2\text{O}_2$  electrostatically bonded to dehydromethionine with a binding energy of 0.34 eV with respect to  $\text{P}_1$  products.

Figure 4 shows the possible H2T reaction pathways at low collision energies, as suggested by the calculations. Hydroperoxides  $\text{H}_1$  and  $\text{H}_2$  have the right properties to serve as intermediates for  $\text{H}_2\text{O}_2$  elimination. The most obvious pathway appears to be reactants  $\rightarrow$  precursor complex  $\rightarrow$  hydroperoxide  $\text{H}_1 \rightarrow$  products. In this pathway,  $\text{H}_1$  has to eliminate  $\text{H}_2\text{O}_2$  via concerted elimination of  $-\text{OOH}$  and one of the methyl hydrogen atoms. Elimination of  $\text{H}_2\text{O}_2$  is common for allylic hydroperoxides in the presence of a labile hydrogen on a neighboring atom.<sup>101,102</sup> However, we were unable to locate a transition state for  $\text{H}_2\text{O}_2$  elimination from  $\text{H}_1$ . We also attempted to locate a product-like geometry following elimination reaction of  $\text{H}_1$ ; however, all product-like geometries converged back to  $\text{H}_1$ . These suggest that  $\text{H}_1$  may not be a good candidate for direct elimination of  $\text{H}_2\text{O}_2$ , presumably because it has a strong hydrogen bonding. A slightly more convoluted pathway is reactants  $\rightarrow$  precursor complex  $\rightarrow \text{H}_1 \rightarrow \text{H}_2 \rightarrow \text{TS}_{\text{H}_2} \rightarrow \text{PC} \rightarrow$  products; i.e.,  $\text{H}_1$  interconverts to  $\text{H}_2$ , followed by elimination of  $\text{H}_2\text{O}_2$  from  $\text{H}_2$  via an activation barrier (0.41 eV above  $\text{H}_2$ ). No other low energy pathways were found leading to  $\text{H}_2\text{O}_2$  elimination from hydroperoxides, although we certainly cannot exclude the possibility that such pathways exist.

The structures of H2T product ions could not be determined by the present experiment. Structures of  $\text{P}_1$ ,  $\text{P}_2$  (a five-membered heterocyclic compound), and  $\text{P}_3$  (a six-membered heterocyclic compound) in Figure 4 are derived from DFT calculations, and their heats of formation ( $\Delta H_{\text{r,ex}}$ ) are −0.55, −0.86, and −1.52 eV, respectively. Among these products,  $\text{P}_3$  is energetically most favorably. In  $\text{P}_1$  and  $\text{P}_2$ , the positive charge is mostly located on the sulfur atom, while part of the positive charge is shifted to the ammonium group in  $\text{P}_3$ . Dissociation of complex PC directly produces  $\text{P}_1$ .  $\text{P}_1$  may interconvert to  $\text{P}_2$  by intramolecular H transfer via  $\text{TS}_{\text{P}_12}$

followed by ring closure; however, the high energy (1.44 eV above the reactants) and tightness of TS\_P12 make this interconversion insignificant at low  $E_{\text{col}}$ . On the other hand, P\_3 can be accessed from P\_1 via a much lower energy barrier, TS\_P13 ( $-0.18$  below the reactants). Therefore, P\_1 and P\_2 are expected to be major products at low energies.

To evaluate whether the complexes and reaction pathways identified in DFT calculations can account for the experimental observations at low  $E_{\text{col}}$ , we used the RRKM program to calculate the lifetime of these complexes as a function of  $E_{\text{col}}$ . For each complex, all decomposition channels indicated by dashed lines in Figure 4 were included. No barrier is expected for decay of precursor complex back to reactants (i.e., no reaction) in excess of the asymptote; thus, an orbiting transition state<sup>103</sup> was assumed. The rotation quantum number  $K$  was treated as active in evaluating the RRKM unimolecular rate constants  $k(E, J)$  so that all  $(2J + 1)$   $K$ -levels are counted,<sup>104</sup> i.e.,

$$k(E, J) = \frac{d \sum_{K=-J}^J G[E - E_0 - E_r^\ddagger(J, K)]}{\sum_{K=-J}^J N[E - E_r(J, K)]}$$

where  $d$  is the reaction path degeneracy,  $G$  is the transition state sum of states,  $N$  is the reactant density of states,  $E_0$  is the unimolecular dissociation threshold, and  $E_r$  and  $E_r^\ddagger$  are the rotational energy for the reactant and the transition state, respectively. The orbital angular momentum  $L$  was estimated from the collision cross section, i.e.,  $L = \mu \cdot v_{\text{rel}} \cdot (\sigma_{\text{collision}}/\pi)^{1/2}$ , where  $\mu$  and  $v_{\text{rel}}$  are the reduced mass and relative velocity of collision partners, respectively. Complexes and TSs were described using scaled frequencies, polarizabilities, and moments of inertia from the DFT calculations. The RRKM lifetime of hydroperoxides is much longer than that of the precursor complex, presumably because the latter is higher in energy. Given the fact that the precursor complex could convert to hydroperoxides, and trajectory simulations showed that hydroperoxides H\_1 and H\_2 could interconvert rapidly, these complexes should be regarded as a single intermediate to account for the overall collision time, with the lifetime being roughly the sum of the calculated lifetimes of precursor complexes H\_1 and H\_2. At collision energies lower than 0.5 eV, the lifetime of this intermediate varies from 10 to 20 ps, longer than the classical rotational period of these complexes which is 4.1–6.8 ps as estimated using the average angular momentum. We note that the intermediate lifetime decreases quickly with increasing  $E_{\text{col}}$ . For comparison, we also calculated the direct “fly by” time required for a 5 Å motion at  $v_{\text{rel}}$  which is 0.58 ps at  $E_{\text{col}} = 0.1$  eV and 0.26 ps at  $E_{\text{col}} = 0.5$  eV. Therefore, the complex lifetime is in the right range and has the right  $E_{\text{col}}$  dependence. The conclusion is that these complexes, if formed efficiently, could significantly mediate the reaction at least for low energies, and the formation of hydroperoxides is expected to be the rate-limiting step in the mechanism. To estimate the significance of H\_1 and H\_2 in the reaction pathway, we calculated the relative populations of H\_1 and H\_2 assuming they are determined by the ratio of the density of states in these two complexes. This assumption is reasonable, since the complexes interconvert rapidly. We used the RRKM program to calculate the complex density of states. It turns out that the ratio of H\_2 to H\_1 is collision energy dependent, and varies between 40:1 and 30:1 at

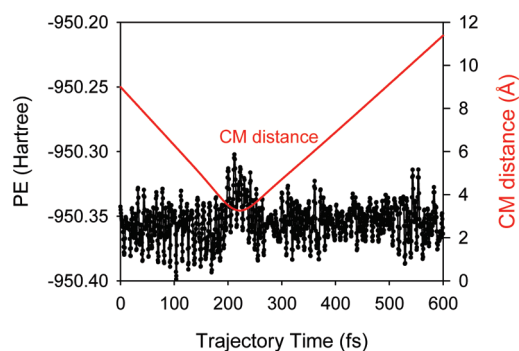


**Figure 5.** A representative plot of nonreactive trajectories, showing the variation of potential energy and center-of-mass distance between  $\text{MetH}^+$  and  $\text{O}_2$  moieties during the trajectory.

$E_{\text{col}} < 1.0$  eV. This suggests that the reaction system spends most of the time as H\_2 at low energies. We note that the RRKM model only gives the results out of the set of complexes but omits consideration of the complex formation probability. Therefore, whether or not the complex-mediated mechanism is important for this system hinges on the efficient formation of complex during collision. The following trajectory simulations have shed light on this question.

**C. Direct Dynamics Trajectory Simulations.** 1. *Nature of the Trajectories.* Before we discuss quasi-classical trajectory simulation results, it is useful to review the nature and time scales of the collisions we are simulating. Trajectories were run at the collision energy of 1.0 eV. Roughly 94% of all 900 trajectories belong to direct nonreactive scattering, resulting in conversion of some collision energy into vibrational and rotational energy (i.e.,  $T \rightarrow E_{\text{int}}$ ). The remaining trajectories either formed electrostatically and hydrogen-bonded weak complexes (i.e., precursor complex in Figure 4, 1.5%) or formed hydroperoxide complexes (H\_1/H\_2, 4.5%). These trajectories are assumed to eventually dissociate to H2T products on the basis of the statistical mechanism discussed above, but it is not practical to propagate these trajectories long enough to observe the decay. No direct H2T reaction was observed at  $E_{\text{col}} = 1.0$  eV. Figures 5 and 6 demonstrate two trajectories representative of nonreactive and reactive collisions, respectively. Both figures show changes of various distances and potential energy (PE) during the trajectory. The CM distance is the distance between the centers of mass of the collision partners. Figure 5 shows a direct, nonreactive scattering, with only one turning point in the relative motion of the reactant centers of mass; i.e., there is no sign of mediation by a complex in this collision. The time scale of the collision is somewhat arbitrary, but three numbers are relevant. The time between trajectory starts and the onset of strong interaction, which depends on reactant orientation, is around 170 fs. The time for reactant approach within 5 Å of the center-of-mass distance is around 130 fs. More importantly, the time period during which  $\text{MetH}^+$  and  $^1\text{O}_2$  interact strongly is around 50 fs, as shown by the potential energy spike beginning at  $t \approx 200$  fs during the trajectory. Figure 6 illustrates a hydroperoxide-forming trajectory, with similar reactant approach time. The  $r(\text{N}-\text{H})$  bond length plotted in the figure corresponds to the distance of the abstracted H atom to the ammonium nitrogen,  $r(\text{S}-\text{O})$  and  $r(\text{O}-\text{H})$  correspond to the S–OO and SOO–H bonds being formed in the hydroperoxide, and  $r(\text{O}-\text{O})$  is the bond length of the  $\text{O}_2$  moiety. The oscillations in bond lengths and PE reflect the vibrations of the reactants or products, including ZPE. We

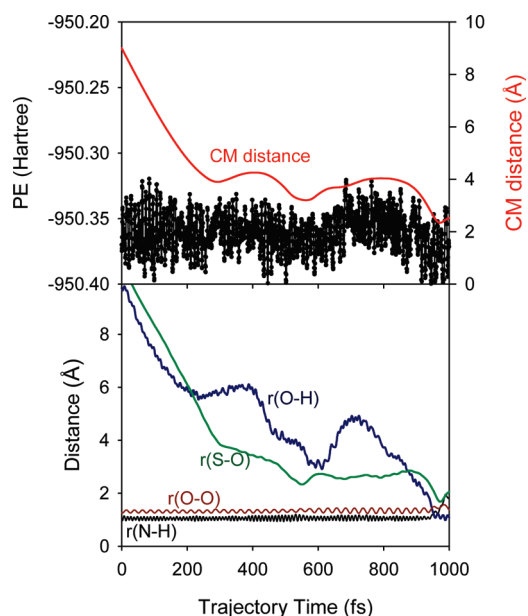


**Figure 6.** A representative plot of hydroperoxide-forming trajectories: (top) the variation of potential energy and center-of-mass distance between  $\text{MetH}^+$  and  $\text{O}_2$  moieties during the trajectory; (bottom) the variation of various bond lengths during the trajectory.

note that the actual hydrogen transfer from  $-\text{NH}_3$  to the peroxide oxygen, defined as the moment when the  $r(\text{N}-\text{H})$  bond extends by more than twice the amplitude of the vibrational fluctuations, occurs almost simultaneously (within a few fs) with the formation of new  $\text{S}-\text{OO}$  and  $\text{SOO}-\text{H}$  bonds; i.e., formation of hydroperoxide is concerted. This is again in agreement with our finding from electronic structure calculations that persulfide of  $\text{MetH}^+$  would converge to a hydroperoxide spontaneously. No dissociation was observed for the hydroperoxide during the trajectory time (1000 fs). It is interesting to note that, in most hydroperoxide-forming trajectories,  $\text{H}_1$  is formed in the initial structure, sometimes isomerizing to  $\text{H}_2$  before trajectory termination.

**2. Trajectory Reaction Cross Section.** Because trajectories were calculated at discrete impact parameters, the H2T reaction cross section,  $\sigma_{\text{H2T}}$ , was calculated using an extended closed trapezoidal approximation<sup>105</sup> to the usual integral form

$$\begin{aligned} \sigma_{\text{H2T}} &= 2\pi \int_0^{b_{\text{max}}} P(b) \\ &\times b \cdot db \cong \pi \sum_{b_i=0.1}^{b_{\text{max}}} [p(b_i) \times b_i + P(b_{i+1}) \times b_{i+1}] \\ &\times (b_{i+1} - b_i) \end{aligned}$$

where  $P(b)$  is the fraction of reactive trajectories at each impact parameter (i.e., opacity function) and  $b_{\text{max}}$  is the maximum value of  $b$  at which reactive trajectories were observed.

In the experiment, the time between  $\text{MetH}^+ - {}^1\text{O}_2$  collision and product ion detection is on the time scale of 10–100  $\mu\text{s}$ , far longer than what could be feasible to simulate. For the purpose of comparison with the experimental cross section, we assume that precursor and hydroperoxide formed at trajectory termination will eventually dissociate to H2T products as rationalized above. We lump all complex-forming trajectories to calculate the H2T opacity function  $P(b)$ . The trajectory opacity functions are given

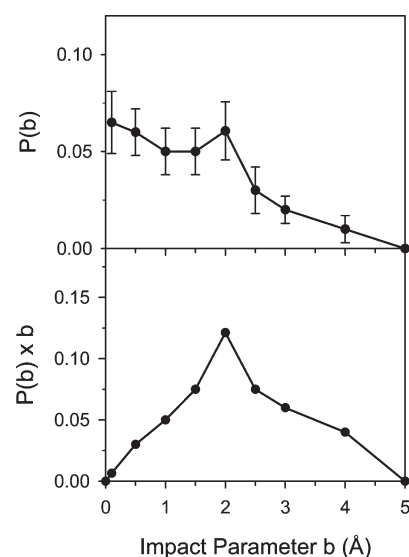


**Figure 7.** Opacity functions for the formation of complexes derived from trajectory simulations.

in Figure 7. The error limits given for  $P(b)$  are usual statistical uncertainties based on the number of total trajectories and reactive trajectories for each impact parameter, and obviously do not include any systematic error. Also shown in Figure 7 is the  $b$ -weighted opacity function  $P(b) \times b$ , which corresponds to the contribution of each range of  $b$  to the reaction cross section. Within the uncertainty,  $P(b)$  has a weak dependence on impact parameter for  $b$  up to 2.0 Å, and then decreases at large  $b$ : falloff is gradual, not sharp. The value of  $b_{\text{max}}$  at which reactive collisions are observed is 4.0 Å. This value is very close to the orientation-averaged hard-sphere collision radius of 3.9 Å. Because the cross section scales like  $P(b) \times b$ , the consequence is that the major contribution to the cross section comes from collisions with  $b$  values between 1.0 and 3.0 Å. The trajectory calculated absolute cross section is  $1.6 \pm 0.9 \text{ \AA}^2$ , comparable to the experimental measured value of  $1.3 \text{ \AA}^2$ . Since the QCT method cannot simulate the physical quenching of  ${}^1\text{O}_2$  via electronic to vibrational energy transfer,<sup>106</sup> trajectories may, to some extent, overestimate reactive collisions. Therefore, taking into account experimental uncertainties (i.e., ion collection efficiency and  ${}^1\text{O}_2$  pressure) and the QCT method limits, the trajectory results are in reasonable agreement with experimental observations. This suggests that trajectories capture the physics necessary to recover the reaction dynamics, and should be useful in interpreting mechanistic details.

**3. Dependence on Collision Orientation.** One of the motivations for doing trajectory simulations is to explore the aspects of reaction dynamics that are not experimentally accessible. In previous trajectory simulations of ion–molecule reactions, we often found that collision orientation is critical for reaction.<sup>37,79,80,82–85</sup> For example, we recently reported trajectory simulations of protonated tyrosine and  ${}^1\text{O}_2$  at  $E_{\text{col}} = 3.0 \text{ eV}$ .<sup>37</sup> Despite the fact that the reaction of  $\text{TyrH}^+ + {}^1\text{O}_2 \rightarrow [\text{Tyr-H}]^+ + \text{H}_2\text{O}_2$  is exoergic, the reaction efficiency is quite low (less than 3%). The reaction occurs either via direct abstraction of two H atoms from protonated tyrosine or through a hydroperoxide-mediated mechanism. Both mechanisms require reactants to be “well-oriented”, and the chance of having a favorable orientation at the time when reactants start to collide is around 8–13%. Therefore, the reaction efficiency is mostly controlled by the reactant parameters and collision orientation.

The fact the reaction opacity functions for  $\text{MetH}^+ + {}^1\text{O}_2$  are roughly independent of  $b$  (Figure 7, from small to intermediate  $b$  range) but significantly less than unity suggests that there exists a dynamical bottleneck that suppresses the reaction. To identify the nature of this bottleneck, we investigated the correlation between reaction probability and collision orientations for  $\text{MetH}^+ + {}^1\text{O}_2$ . To quantify the dependence of reactivity on orientation, we need to define a critical point in each trajectory where orientation can be examined. Here, we take the critical point to be the first time when  $\text{O}_2$  approaches within 3.0 Å of the S atom of  $\text{MetH}^+$ . For nonreactive trajectories which never reach this critical point, we characterize the collision orientation at the turning point of the inter-reactant separation. Strong orientation dependence was found for  $\text{MetH}^+ + {}^1\text{O}_2$ . All complex-forming trajectories must have  $\text{O}_2$  approach both the S atom and ammonium group simultaneously, forming precursor and hydroperoxide. At  $b \leq 2.0$  Å, only  $\sim 20\%$  of collisions have such orientations at the time when reactants start to collide (and 40% of these form complexes). The balance of collisions either have  $\text{O}_2$  attack the backbone of methionine (33% of total trajectories) or approach the  $-\text{CH}_2\text{CH}_2\text{SCH}_3$  group from the back side of the ammonium group (47% of total trajectories). The latter two lead to nonreactive scatterings. Trajectory visualization suggests that the critical point is late enough in the trajectory that there is not enough time for significant orientation steering before forming any complex; therefore, the narrow range of optimal orientations could explain the low reaction efficiency observed in experiment at  $E_{\text{col}} = 1.0$  eV. Trajectories show that collisions exclusively between  $\text{O}_2$  and the S atom, i.e., without attacking the ammonium group at the same time, do not lead to reactive trajectories. This demonstrates that a precursor complex with a hydrogen bond between  $\text{NH}_3^+$  and  $\text{O}_2$  is essential for the early stage of the reaction.

Because the trajectories were terminated at intermediates, we were unable to evaluate the product energy partitioning for reactive trajectories. For nonreactive trajectories, mean product recoil energies  $\langle E_{\text{recoil}} \rangle$  are calculated to be 0.24, 0.25, 0.28, 0.29, 0.33, 0.38, 0.45, 0.64, and 0.84 eV and product scattering angles are calculated to be 109, 108, 101, 88, 83, 67, 52, 28, and  $22^\circ$  for  $b = 0.1, 0.5, 1.0, 1.5, 2.0, 2.5, 3.0, 4.0,$  and  $5.0$  Å, respectively. It is expected from the line-of-centers model<sup>59</sup> that the values of  $\langle E_{\text{recoil}} \rangle$  increase with increasing  $b$ , because the strength of collision interaction becomes weak and consequently the  $T \rightarrow E_{\text{int}}$  energy transfer decreases monotonically at large  $b$ . For nonreactive trajectories,  $b$ -averaged values of  $\langle E_{\text{recoil}} \rangle$  and  $\langle E_{\text{rot}} \rangle$  are 0.55 and 0.24 eV; thus, most  $T \rightarrow E_{\text{int}}$  is partitioned to product vibrational energy. We note that all trajectories have total energy conserved to the sum of individual electronic energies and rovibrational energies of  ${}^1\text{MetH}^+$  and  ${}^1\text{O}_2$ . This implies that the nonadiabatic transition between different electronic states has been safely avoided in simulations. Another problem is that this system is likely a candidate for multiconfiguration wave functions. We tested this problem by running single point CASSCF(10,10) calculations for all geometries explored in the trajectories and found that the Hartree–Fock configuration is strongly dominant, i.e., that multifunction wave functions should not be an issue in this system.

#### IV. CONCLUSIONS

The present study employs guided ion beam tandem mass spectrometry to determine the reaction product, cross section, and collision energy dependence for the reaction of protonated

methionine with electronically excited singlet molecular oxygen ( ${}^1\Delta_g$ ). DFT calculations were carried out to identify the reaction coordinate (including reactants, intermediate complexes, transition states, and various products), analyze thermodynamics and energy barriers, as well as provide insight into the different types of stabilization of protonated species upon oxidation. DFT calculations demonstrate that the  $-\text{SOO}$  group of  $\text{MetOOH}^+$  has a higher proton affinity than the amino group, making methionine hydroperoxide the most stable intermediate. Extensive quasi-classical direct dynamics trajectory simulations were performed at a collision energy of 1.0 eV. Trajectories demonstrate the importance of a complex-mediated mechanism for H2T even at a high  $E_{\text{col}}$ , and reveal a number of interesting dynamics features including sharp orientation dependence for reaction.

One of the most interesting results is that gas-phase reaction of protonated methionine with “short-lived” singlet molecular oxygen could produce a “long-lived” hydrogen peroxide, which can diffuse to distant targets in biological systems. A similar reaction has been observed for protonated tyrosine and singlet oxygen<sup>37</sup> but with a much lower reaction efficiency. The different reaction efficiencies for these two protonated amino acids may be rationalized by considering the nature of their reaction intermediates. For the reaction of protonated tyrosine with singlet oxygen, the most likely route (with the lowest barrier) is the formation of various endoperoxides via 2 + 4 cycloaddition of  ${}^1\text{O}_2$  to the benzene ring. This process is reversible;<sup>107,108</sup> i.e., endoperoxides may decay back to reactants and physically quench singlet oxygen via electronic-to-electronic and/or electronic-to-vibrational energy transfer.<sup>109</sup> Only a small fraction of collisions of  $\text{TyrH}^+ + {}^1\text{O}_2$  form hydroperoxide intermediates which finally lead to chemical reactions.<sup>37</sup> In contrast, due to the higher proton affinity of the  $-\text{SOO}$  group, hydroperoxide intermediates are energetically favorable and form overwhelmingly in the reaction of  $\text{MetH}^+$  with  ${}^1\text{O}_2$ . This becomes a key factor in determining the late stage of the reaction and is responsible for the high reaction efficiency of  $\text{MetH}^+ + {}^1\text{O}_2$ , because the hydroperoxide traps the  $\text{O}_2$  moiety in the middle of an intramolecular ionic hydrogen bond  $\text{SOOH} \cdots \text{NH}_2$ , which makes physical quenching of  ${}^1\text{O}_2$  less favorable.

#### AUTHOR INFORMATION

##### Corresponding Author

\*E-mail: jianbo.liu@qc.cuny.edu.

#### ACKNOWLEDGMENT

This work was supported by the National Science Foundation CAREER Award (CHE-0954507), Queens College Research Enhancement Funds, and PSC-CUNY Research Awards. Y.F. is the recipient of the CUNY Doctoral Student Research Grant and Research Excellence Award in 2010. A.B. acknowledges support by Queens College Undergraduate/Mentoring Education Initiative. The authors appreciate Al Viggiano (Air Force Research Laboratory) for help with setting up the chemical singlet oxygen generator and Alexander Greer (CUNY Brooklyn College) for useful discussions.

#### REFERENCES

- (1) Frimer, A. A. *Singlet Oxygen, Vol I, Physical-Chemical Aspects*; CRC Press: Boca Raton, FL, 1985.

- (2) Frimer, A. A. *Singlet Oxygen, Vol II, Reaction Modes and Products, Part 1*; CRC Press: Boca Raton, FL, 1985.
- (3) Frimer, A. A. *Singlet O<sub>2</sub>, Vol III, Reaction Modes and Products, Part 2*; CRC Press: Boca Raton, FL, 1985.
- (4) Frimer, A. A. *Singlet O<sub>2</sub>, Vol IV, Polymers and Biomolecules*; CRC Press: Boca Raton, FL, 1985.
- (5) Sawyer, D. T. *Oxygen Chemistry*; Oxford University Press: New York, 1991.
- (6) Ogilby, P. R. *Chem. Soc. Rev.* **2010**, 39, 3181.
- (7) Davies, M. J. *Biochim. Biophys. Acta* **2005**, 1703, 93.
- (8) Palumbo, G. *Expert Opin. Drug Delivery* **2007**, 4, 131.
- (9) McGregor, K. G.; Anastasio, C. *Atmos. Environ.* **2001**, 35, 1091.
- (10) Davies, M. J. *Biochem. Biophys. Res. Commun.* **2003**, 305, 761.
- (11) Davies, M. J. *Photochem. Photobiol. Sci.* **2004**, 3, 17.
- (12) Stadtman, E. R.; Remmen, H. V.; Richardson, A.; Wehr, N. B.; Levine, R. L. *Biochim. Biophys. Acta* **2005**, 1703, 135.
- (13) Delaye, L.; Becerra, A.; Orgel, L.; Lazcano, A. *J. Mol. Evol.* **2007**, 64, 15.
- (14) Mace, K. A.; Duce, R. A.; Tindale, N. W. *J. Geophys. Res.* **2003**, 108, 4338.
- (15) Mader, B. T.; Yu, J. Z.; Xu, J. H.; Li, Q. F.; Hu, W. S.; Flagan, R. C.; Seinfeld, J. H. *J. Geophys. Res.* **2004**, 109, D06206.
- (16) Matsumoto, K.; Uematsu, M. *Atmos. Environ.* **2005**, 39, 2163.
- (17) Leck, C.; Bigg, E. K. *Geophys. Res. Lett.* **1999**, 26, 3577.
- (18) Anastasio, C.; McGregor, K. G. *Atmos. Environ.* **2001**, 35, 1079.
- (19) Schweitzer, C.; Schmidt, R. *Chem. Rev.* **2003**, 103, 1685.
- (20) Weil, L.; Gordon, W. G.; Buchert, A. R. *Arch. Biochem.* **1951**, 33, 90.
- (21) Spikes, J. D.; MacKnight, M. L. *Ann. N. Y. Acad. Sci.* **1970**, 171, 149.
- (22) Cohen, S. G.; Ojanpera, S. *J. Am. Chem. Soc.* **1975**, 97, 5633.
- (23) Sysak, P. K.; Foote, C. S.; Ching, T.-Y. *Photochem. Photobiol.* **1977**, 26, 19.
- (24) Rougee, M.; Bensasson, R. V.; Land, E. J.; Pariente, R. *Photochem. Photobiol.* **1988**, 47, 485.
- (25) Bertolotti, S. G.; Garcia, N. A.; Arguello, G. A. *J. Photochem. Photobiol., B* **1991**, 10, 57.
- (26) Stadtman, E. R.; Berlett, B. S. *Free Radical Toxicol.* **1997**, 71.
- (27) Marciniak, B.; Hug, G. L.; Bobrowski, K.; Kozubek, H. *J. Phys. Chem.* **1995**, 99, 13560.
- (28) Hug, G. L.; Bobrowski, k.; Kozubek, H.; Marciniak, B. *Photochem. Photobiol.* **1998**, 68, 785.
- (29) Barata-Vallejo, S.; Ferreri, C.; Postigo, A.; Chatgililoglu, C. *Chem. Res. Toxicol.* **2010**, 23, 258.
- (30) Lewis, C.; Scouten, W. H. *Biochim. Biophys. Acta* **1976**, 444, 326.
- (31) Lewis, C.; Scouten, W. H. *J. Chem. Educ.* **1976**, 53, 394.
- (32) Zamadar, M.; Aebisher, D.; Greer, A. *J. Phys. Chem. B* **2009**, 113, 15803.
- (33) Aebisher, D.; Zamadar, M.; Mahendran, A.; Ghosh, G.; McEntee, C.; Greer, A. *Photochem. Photobiol.* **2010**, 86, 890.
- (34) Yamashita, M.; Fenn, J. B. *J. Phys. Chem.* **1984**, 88, 4451.
- (35) Fenn, J. B.; Mann, M.; Meng, C. K.; Wong, S. F.; Whitehouse, C. M. *Science* **1989**, 246, 64.
- (36) Gerlich, D. Inhomogeneous RF fields: A versatile tool for the study of processes with slow ions. In *State-Selected and State-to-State Ion–Molecule Reaction Dynamics. Part I. Experiment*; Ng, C. Y., Baer, M., Eds.; John Wiley & Sons, Inc.: New York, 1992; Vol. 82, p 1.
- (37) Fang, Y.; Liu, J. *J. Phys. Chem. A* **2009**, 113, 11250.
- (38) Fehsenfeld, F. C.; Albritton, D. L.; Burt, J. A.; Schiff, H. I. *Can. J. Chem.* **1969**, 47, 1793.
- (39) Schmitt, R. J.; Bierbaum, V. M.; DePuy, C. H. *J. Am. Chem. Soc.* **1979**, 101, 6443.
- (40) Bierbaum, V. M.; Schmitt, R. J.; DePuy, C. H. *Environ. Health Perspect.* **1980**, 36, 119.
- (41) Grabowski, J. J.; Van Doren, J. M.; DePuy, C. H.; Bierbaum, V. M. *J. Chem. Phys.* **1984**, 80, 575.
- (42) Dotan, I.; Barlow, S. E.; Ferguson, E. E. *Chem. Phys. Lett.* **1985**, 121, 38.
- (43) Upschulte, B. L.; Marinelli, W. J.; Green, B. D. *J. Phys. Chem.* **1994**, 98, 837.
- (44) Midey, A.; Dotan, I.; Lee, S.; Rawlins, W. T.; Johnson, M. A.; Viggiano, A. A. *J. Phys. Chem. A* **2007**, 11, 5218.
- (45) Midey, A.; Dotan, I.; Viggiano, A. A. *J. Phys. Chem. A* **2008**, 112, 3040.
- (46) Midey, A. J.; Dotan, I.; Viggiano, A. A. *Int. J. Mass Spectrom.* **2008**, 273, 7.
- (47) Midey, A.; Dotana, I.; Seeley, J. V.; Viggiano, A. A. *Int. J. Mass Spectrom.* **2009**, 280, 6.
- (48) Viggiano, A. A.; Midey, A.; Eyet, N.; Bierbaum, V. M.; Troe, J. *J. Chem. Phys.* **2009**, 131, 094303/1.
- (49) Eyet, N.; Midey, A.; Bierbaum, V. M.; Viggiano, A. A. *J. Phys. Chem. A* **2010**, 114, 1270.
- (50) Eyet, N.; Viggiano, A. A. *J. Phys. Chem. A* **2010**, 114, 7506.
- (51) Marcus, R. A. *J. Chem. Phys.* **1952**, 20, 359.
- (52) Fang, Y.; Bennett, A.; Liu, J. *Int. J. Mass Spectrom.* **2010**, 293, 12.
- (53) Fang, Y.; Bennett, A.; Liu, J. *Phys. Chem. Chem. Phys.* **2011**, 13, 1466.
- (54) Chowdhury, S. K.; Katta, V.; Chait, B. T. *Rapid Commun. Mass Spectrom.* **1990**, 4, 81.
- (55) Moision, R. M.; Armentrout, P. B. *J. Am. Soc. Mass Spectrom.* **2007**, 18, 1124.
- (56) Krutchinsky, A. N.; Chernushevich, I. V.; Spicer, V. L.; Ens, W.; Standing, K. G. *J. Am. Soc. Mass Spectrom.* **1998**, 9, 569.
- (57) Douglas, D. J.; French, J. B. *J. Am. Soc. Mass Spectrom.* **1992**, 3, 398.
- (58) Moision, R. M.; Armentrout, P. B. *J. Phys. Chem. A* **2006**, 110, 3933.
- (59) Levine, R. D.; Bernstein, R. B. *Molecular Reaction Dynamics and Chemical Reactivity*; Oxford University Press: New York, 1987.
- (60) Liu, J.; Van Devener, B.; Anderson, S. L. *J. Chem. Phys.* **2002**, 116, 5530.
- (61) Armentrout, P. B. *Int. J. Mass Spectrom.* **2000**, 200, 219.
- (62) Ervin, K. M.; Armentrout, P. B. *J. Chem. Phys.* **1985**, 83, 166.
- (63) Ogryzlo, E. A. Gaseous Singlet Oxygen. In *Singlet Oxygen*; Wasserman, H. H., Murray, R. W., Eds.; Academic Press, Inc.: New York, 1979; p 35.
- (64) Savin, Y. V.; Goryachev, L. V.; Adamenkov, Y. A.; Rakhimova, T. V.; Mankelevich, Y. A.; Popov, N. A.; Adamenkov, A. A.; Egorov, V. V.; Ilyin, S. P.; Kolobyanin, Y. V.; Kudryashov, E. A.; Rogozhnikov, G. S.; Vyskubenko, B. A. *J. Phys. D: Appl. Phys.* **2004**, 37, 3121.
- (65) Popović, S.; Rašković, M.; Kuo, S. P.; Vušković, L. *J. Phys.: Conf. Ser.* **2007**, 86, 012013.
- (66) Seliger, H. H. *Anal. Biochem.* **1960**, 1.
- (67) Khan, A.; Kasha, M. *J. Chem. Phys.* **1963**, 39, 2105.
- (68) McDermott, W. E.; Pchelkin, N. R.; Benard, D. J.; Bousek, R. R. *Appl. Phys. Lett.* **1978**, 32, 469.
- (69) Lafferty, W. J.; Solodov, A. M.; Lugez, C. L.; Fraser, G. T. *Appl. Opt.* **1998**, 37, 2264.
- (70) Newman, S. M.; Lane, I. C.; Orr-Ewing, A. J.; Newnham, D. A.; Ballard, J. *J. Chem. Phys.* **1999**, 110, 10749.
- (71) Duo, L.; Cui, T.; Wang, Z.; Chen, W.; Yang, B.; Sang, F. *J. Phys. Chem. A* **2001**, 105, 281.
- (72) Troe, J. *Chem. Phys. Lett.* **1985**, 122, 425.
- (73) Frisch, M. J.; Trucks, G. W.; Schlegel, H. B.; Scuseria, G. E.; Robb, M. A.; Cheeseman, J. R.; Montgomery, J. A., Jr.; Vreven, T.; Kudin, K. N.; Burant, J. C.; Millam, J. M.; Iyengar, S. S.; Tomasi, J.; Barone, V.; Mennucci, B.; Cossi, M.; Scalmani, G.; Rega, N.; Petersson, G. A.; Nakatsuji, H.; Hada, M.; Ehara, M.; Toyota, K.; Fukuda, R.; Hasegawa, J.; Ishida, M.; Nakajima, T.; Honda, Y.; Kitao, O.; Nakai, H.; Klene, M.; Li, X.; Knox, J. E.; Hratchian, H. P.; Cross, J. B.; Bakken, V.; Adamo, C.; Jaramillo, J.; Gomperts, R.; Stratmann, R. E.; Yazyev, O.; Austin, A. J.; Cammi, R.; Pomelli, C.; Ochterski, J. W.; Ayala, P. Y.; Morokuma, K.; Voth, G. A.; Salvador, P.; Dannenberg, J. J.; Zakrzewski, V. G.; Dapprich, S.; Daniels, A. D.; Strain, M. C.; Farkas, O.; Malick, D. K.; Rabuck, A. D.; Raghavachari, K.; Foresman, J. B.; Ortiz, J. V.; Cui, Q.; Baboul, A. G.; Clifford, S.; Cioslowski, J.; Stefanov, B. B.; Liu, G.;

- Liashenko, A.; Piskorz, P.; Komaromi, I.; Martin, R. L.; Fox, D. J.; Keith, T.; Al-Laham, M. A.; Peng, C. Y.; Nanayakkara, A.; Challacombe, M.; Gill, P. M. W.; Johnson, B.; Chen, W.; Wong, M. W.; Gonzalez, C.; Pople, J. A. *Gaussian 03*, rev. E.01; Gaussian, Inc: Wallingford, CT, 2004.
- (74) Foresman, J. B.; Frisch, A. *Exploring Chemistry with Electronic Structure Methods*, 2nd ed.; Gaussian, Inc: Pittsburgh, PA, 2000.
- (75) Zhu, L.; Hase, W. L. A General RRKM Program (QCPE 644), Quantum Chemistry Program Exchange; Chemistry Department, University of Indiana: Bloomington, IN, 1993.
- (76) Hase, W. L.; Bolton, K.; de Sainte Claire, P.; Duchovic, R. J.; Hu, X.; Komornicki, A.; Li, G.; Lim, K.; Lu, D.; Peslherbe, G. H.; Song, K.; Swamy, K. N.; Vande Linde, S. R.; Varandas, A.; Wang, H.; Wolf, R. J. *VENUS99: A general chemical dynamics computer program*; Texas Tech University: Lubbock, TX, 1999.
- (77) Bakken, V.; Millam, J. M.; Schlegel, H. B. *J. Chem. Phys.* **1999**, *111*, 8773.
- (78) Bacskay, G. B. *Chem. Phys.* **1981**, *61*, 385.
- (79) Liu, J.; Uselman, B.; Boyle, J.; Anderson, S. L. *J. Chem. Phys.* **2006**, *125*, 133115.
- (80) Boyle, J. M.; Liu, J.; Anderson, S. L. *J. Phys. Chem. A* **2009**, *113*, 3911.
- (81) Laaksonen, L. *gOpenMol*, 3.0 ed.; Center for Scientific Computing: Espoo, Finland, 2002; available at [www.csc.fi/gopenmol/](http://www.csc.fi/gopenmol/).
- (82) Liu, J.; Song, K.; Hase, W. L.; Anderson, S. L. *J. Chem. Phys.* **2003**, *119*, 3040.
- (83) Liu, J.; Song, K.; Hase, W. L.; Anderson, S. L. *J. Am. Chem. Soc.* **2004**, *126*, 8602.
- (84) Liu, J.; Song, K.; Hase, W. L.; Anderson, S. L. *J. Phys. Chem. A* **2005**, *109*, 11376.
- (85) Liu, J.; Anderson, S. L. *Phys. Chem. Chem. Phys.* **2009**, *11*, 8721.
- (86) Untch, A.; Schinke, R.; Cotting, R.; Huber, J. R. *J. Chem. Phys.* **1993**, *99*, 9553.
- (87) Miller, W. H. *J. Chem. Soc., Faraday Trans.* **1997**, *93*, 685.
- (88) Kulik, W.; Heerma, W. *Biomed. Environ. Mass Spectrom.* **1988**, *15*, 419.
- (89) Lagerwed, F. M.; Weert, M. v. d.; Heerma, W.; Haverkamp, J. *Rapid Commun. Mass Spectrom.* **1996**, *10*, 1905.
- (90) Dookeran, N. N.; Yalcin, T.; Harrison, A. G. *J. Mass Spectrom.* **1996**, *31*, 500.
- (91) O'Hair, R. A. J.; Reid, G. E. *Eur. Mass Spectrom.* **1999**, *5*, 325.
- (92) Rogalewicz, F. o.; Hoppilliard, Y.; Ohanessian, G. *Int. J. Mass Spectrom.* **2000**, *195–196*, 565.
- (93) Lavine, T. F. *Fed. Proc.* **1945**, *4*, 96.
- (94) Leach, A. R. *Molecular modeling: Principles and applications*; Pearson, Prentice Hall: Harlow, England, 2001.
- (95) Desaphy, S.; Malosse, C.; Bouchoux, G. *J. Mass Spectrom.* **2008**, *43*, 116.
- (96) Borisov, Y. A.; Zolotarev, Y. A.; Laskatelev, E. V.; Myasoedov, N. F. *Russ. Chem. Bull.* **1998**, *47*, 1442.
- (97) Bleiholder, C.; Suhai, S.; Paizs, B. *J. Am. Soc. Mass Spectrom.* **2006**, *17*, 1275.
- (98) Lioe, H.; O'Hair, R. A. J.; Gronert, S.; Austin, A.; Reid, G. E. *Int. J. Mass Spectrom.* **2007**, *267*, 220.
- (99) Carl, D. R.; Cooper, T. E.; Oomens, J.; Steillb, J. D.; Armentrout, P. B. *Phys. Chem. Chem. Phys.* **2010**, *12*, 3384.
- (100) Lioe, H.; O'Hair, R. A. J.; Reid, G. E. *J. Am. Soc. Mass Spectrom.* **2004**, *15*, 65.
- (101) Chen, Y.-Z.; Wu, L.-Z.; Peng, M.-L.; Zhang, D.; Zhang, L.-P.; Tung, C.-H. *Tetrahedron* **2006**, *62*, 10688.
- (102) Morgan, P. E.; Dean, R. T.; Davies, M. J. *Free Radical Biol. Med.* **2008**, *36*, 484.
- (103) Rodgers, M. T.; Ervin, K. M.; Armentrout, P. B. *J. Chem. Phys.* **1997**, *106*, 4419.
- (104) Zhu, L.; Hase, W. L. *Chem. Phys. Lett.* **1990**, *175*, 117.
- (105) Press, W. H.; Teukolsky, S. A.; Vetterling, W. T.; Flannery, B. P. *Numerical Recipes in C. The Art of Scientific Computing*, 2nd ed.; Cambridge Univ. Press: Cambridge, U.K., 1992.
- (106) Wilkinson, F.; Helman, W. P.; Ross, A. B. *J. Phys. Chem. Ref. Data* **1995**, *24*, 663.
- (107) Moureu, C.; Dufraisse, C.; Dean, P. M. *C. R. Acad. Sci.* **1926**, *182*, 1584.
- (108) Martinez, G. R.; Garcia, F.; Catalani, L. H.; Cadet, J.; Oliveira, M. C. B.; Ronsein, G. E.; Miyamoto, S.; Medeiros, M. H. G.; Masciod, P. D. *Tetrahedron* **2006**, *62*, 10762.
- (109) Farmilo, A.; Wilkinson, F. *Photochem. Photobiol.* **1973**, *18*, 447.